ROYAL SOCIETY OF CHEMISTRY

PAPER

Acoustic shock wave driven dynamic recrystallization induced reversible rod-to-cube morphology transition in CdS: preserving structural integrity with optical modifications

F. Irine Maria Bincy,[a] Oviya Sekar,[a] Kannappan Perumal,[a] Ikhyun Kim [ID] *[b] and S. A. Martin Britto Dhas [ID] *[a,b]

Cadmium sulfide (CdS) is a promising semiconductor with a narrower bandgap, making it highly suitable for optoelectronic and energy storage applications. However, its response to extreme conditions, such as acoustic shock waves, remains unexplored. In this study, CdS samples were subjected to varying shock pulses such as 100, 200, 300, and 400 at a transient pressure of 0.59 MPa and a temperature of 520 K, with a Mach number of 1.5, to investigate structural, optical, and morphological modifications. Analytical techniques, including X-ray diffraction (XRD), Raman spectroscopy, UV-Vis Diffuse Reflectance Spectroscopy (DRS), Photoluminescence (PL) spectroscopy, and Field-Emission Scanning Electron Microscopy (FE-SEM), were employed for comprehensive analysis. XRD and Raman results confirm that the structure remains stable up to 400 shock pulses, with only a minor peak shift observed at 300 shock pulses and, at 400 shock pulses which subsequently reverts to its original position. Optical studies reveal a reversible bandgap shift from 2.37 eV to 2.24 eV, while the PL emission peak shifts from 518 nm to 528 nm and reverts to its original position at 400 shock pulses. Most interestingly, FE-SEM analysis reveals a morphological transition, and the rod morphology evolves into a cube morphology at 300 shock pulses due to shock wave-induced dynamic recrystallization. Remarkably, at 400 shock pulses, the morphology reverts to its original rod morphology, highlighting the reversibility of morphology. These results highlight the critical role of dynamic recrystallization in enabling morphology modulation without structural phase alteration. This study establishes acoustic shock waves as a promising pathway to tune both optical properties and morphology of materials while preserving their structural integrity, offering new directions for functional material design and processing.

Introduction

In the modern era, cadmium sulfide (CdS) stands as a prominent II–VI semiconductor with wide-ranging potential[1] due to its narrow bandgap with high conduction band potential contributing to unique optical properties in the visible region.[2–4] CdS has numerous applications like light-emitting diodes,[5,6] hydrogen evolution,[7] photovoltaic cells, catalytic properties,[8,9] photodetectors,[10,11] solar cells, optoelectronic applications,[12] and bio tagging molecules when functionalized with biomolecules.[13] Furthermore, the distinctive photochemical and photophysical properties of CdS have led to extensive research

on its potential for dye effluent treatment.[14] Therefore, CdS continues to attract widespread research interest due to its properties, including its crystal structure, optical properties, and morphology, which play a vital role in its performance. Hence, ongoing efforts focus on optimizing these factors for improved efficiency.[15–19] Structural tunability plays a vital role in determining a material's stability and performance, while optical properties are closely linked to factors such as bandgaps and light absorption. Morphology tunability, influenced by both internal factors like symmetry and external conditions such as temperature, additives, and solvents, further impacts these properties. Given its significance across industries such as pharmaceuticals and petrochemicals, precise control over materials' morphology is essential for optimizing both structural and optical performance in various applications.[20]

Over the past few decades, CdS has been synthesized and investigated by conventional and unconventional methods. Under conventional methods, its structure, optical properties,

[a]*Shock Wave Research Laboratory, Department of Physics, Abdul Kalam Research Center, Sacred Heart College, Tirupattur, Affiliated to Thiruvalluvar University, Tamil Nadu, 635 601, India. E-mail: martinbritto@shctpt.edu*
[b]*Department of Mechanical Engineering, Keimyung University, Daegu 42601, Republic of Korea. E-mail: kimih@kmu.ac.kr*

and morphology are influenced by factors such as the different synthesis methods, reaction temperature, reaction time, and raw materials and by many methods such as hydrothermal, sol–gel, solvothermal,[21] hot wall deposition,[22] spray pyrolysis,[23] cathodic electrodeposition,[24] thermal evaporation,[25] and chemical bath deposition methods.[26] Unconventional methods involve static high pressure,[27] laser shock waves,[28] gamma irradiation,[29] and acoustic shock waves.[30,31] Few literature reports on conventional methods indicate that the annealing temperature plays a crucial role in modifying the structural, optical, and morphological properties of CdS. Higher temperatures induce phase transformations, leading to the formation of $CdSO_4$ and CdO. Morphological changes, such as sintering, result in larger, smooth, and irregular particles. Studies also reveal that annealing can tune optical properties by adjusting the bandgap and light absorption. TG/DSC analyses further confirm these transformations, emphasizing the significance of thermal treatment in tailoring CdS properties.[32] Under unconventional methods, CdS undergoes a wurtzite-to-rock-salt phase transition around 25–27 kbars, which significantly alters its structural, electronic, and optical properties. This pressure-induced phase transformation changes the coordination geometry from tetrahedral to octahedral, reducing the band gap from 2.54 eV (direct) to 1.55 eV (indirect). The transition completely quenches photoluminescence while enhancing electrical conductivity. This transition creates permanent defects upon pressure release, enabling applications in pressure sensors and tunable optoelectronics.[33] High-temperature and high-pressure investigations on CdS using *in situ* synchrotron radiation X-ray diffraction confirm that a complete phase transition was observed from the wurtzite (WZ) to the rock-salt (RS) phase at 2.6 GPa. The RS phase remains stable up to 21.9 GPa, and the transition is fully reversible upon decompression. The study further highlights that the bulk modulus of RS CdS is influenced by the cation radius and electronegativity, which play a crucial role in its mechanical stability.[34]

Unlike conventional methods, such acoustic shock wave methods have gained prominence in solid-state material research, especially since the advent of the 21st century and the invention of tabletop shock tubes.[35] Conventional synthesis techniques are time-consuming, often leading to impurities and prolonged processing. Additionally, most conventional methods involve heat treatments, such as thermal annealing, used to modify the material properties. However, CdS tends to oxidize, forming sulfates and oxides, which can impact its stability and performance.[36] In contrast, unconventional methods like high-pressure techniques achieve compression within minutes to hours, offering a higher compression rate. Acoustic shock waves, however, operate on a broader timescale, from milliseconds to microseconds, making them a versatile alternative method. This ongoing exploration highlights the growing interest in acoustic shock wave studies, positioning them as a promising avenue for material research.[37,38] Several studies on acoustic shock waves have reported diverse effects on materials by using a tabletop semi-automatic Reddy tube. For instance, Bi_2Te_3[39] and ZnTe[40] exhibited reversible morphological changes, but these were accompanied by structural transitions. Similarly, CdO undergoes

a transition from the NaCl-type structure (B1 phase) to the CsCl-type structure (B2 phase), with a change in morphology from a rod shape to a rectangular shape.[41] In the case of In_4Se_3 and α-In_2Se_3, a mixed phase transformed into pure rhombohedral α-In_2Se_3, showing phase stabilization and optical modification without any morphological changes.[42] Meanwhile, Bi_2Se_3[43] and BiS_2[44] demonstrated structural stability and allowed for optical tuning without altering the morphology. Notably, by acoustic shock wave treatment, none of these studies reported reversible morphological changes with tunable optical properties without accompanying structural transitions, highlighting the uniqueness of the present findings.

To date, there are no available studies investigating the structural, optical, and morphological behavior of CdS under acoustic shock waves. To address this, the present work systematically investigates how CdS responds to controlled shock wave exposure, providing new insights into its structural stability, optical modification, and morphology tunability. CdS samples were subjected to acoustic shock waves with varying shock pulse counts, such as 100, 200, 300, and 400 shock pulses, to examine progressive changes in their structural and optical properties, and surface morphology. The shock waves were applied at a pressure of 0.59 MPa, a temperature of 520 K, and a Mach number of 1.5, ensuring a well-defined impact on the material. This study reveals that acoustic shock waves can reversibly tune the optical properties and morphology of materials without inducing structural phase changes. By demonstrating a reversible rod-to-cube morphology transition in CdS, we introduce a new, non-destructive approach to control material functionality. These findings highlight acoustic shock wave treatment as a powerful method for designing adaptable materials for applications in optoelectronics, energy storage, and systems requiring high structural resilience. This pioneering investigation presents the detailed account of CdS behavior under acoustic shock wave exposure, addressing a significant gap in the current literature.

Shock loading experiment

Cadmium sulfide (CdS) was procured from SRL with 99.9% purity, India, and utilized without any additional purification for analysis under acoustic shock wave exposure. The shock waves were generated using a tabletop semi-automatic Reddy tube. A pictorial depiction of the semi-automatic Reddy tube is illustrated in Fig. 1. The experimental shock tube setup consists of a three sections from that driver section and a driven section, which are cylindrical seamless tubes of 48 cm and 33 cm length, respectively. Both sections have an inner diameter of 1.5 cm. A diaphragm separates the two sections and is fitted with an 80 GSM diaphragm, which is manually inserted into the diaphragm section. The powder samples were placed in a specially designed pouch made of a polyethylene sheet, with dimensions of $10 \times 10 \times 1$ mm^3. The samples were tightly packed without any air bubbles or trapped air and then securely sealed to avoid oxidation during the shock exposure and bursting of the sample pouch. The sealed pouch was firmly mounted in a stainless-steel sample holder,
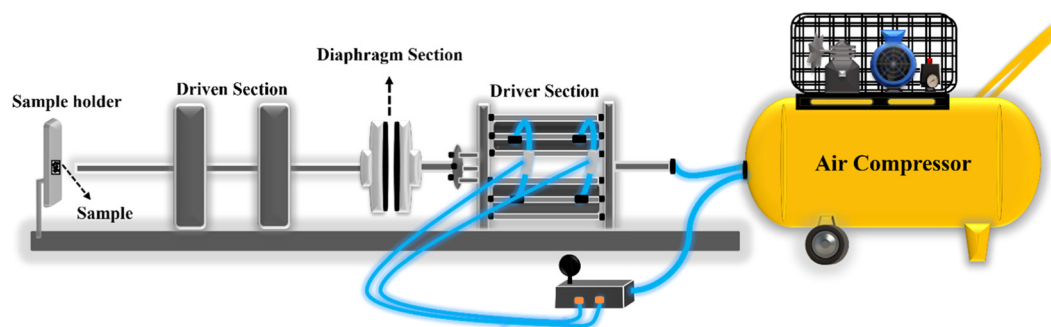
Fig. 1 Pictorial depiction of the tabletop semi-automatic Reddy tube setup.

positioned 1 cm away from the open end of the driven section, aligned along it's axis to ensure uniform shock exposure. When the pressure in the driver section reached the critical threshold, the diaphragm ruptured, generating shock waves. The CdS samples were exposed to four series of shock pulses, such as 100, 200, 300, and 400. The Mach number, transient pressure, and temperature per shock pulses were measured using two piezoelectric PCB transducers (Model No. 113B26) that were placed 39 cm apart along the driven section with a sensitivity of 1.465 mV kPa^{-1} and a linearity error of 1%. These calibrations guaranteed precise and repeatable transient pressure measurements, serving as a dependable reference for analyzing the impact of shock pulses on the samples. The Mach number was calculated using the formula, $M = V/a$, where V represents the velocity of the object or shock wave (m s^{-1}), and a represents the speed of sound in the medium (m s^{-1}). To determine the shock velocity (V), two piezoelectric PCB transducers are placed in the driver section at a known distance apart. By simultaneously measuring the pressure signals and their corresponding time-lag between the sensors using a storage oscilloscope, the speed of the shock pulses can be accurately determined. The time response for each shock wave exposure duration was found to be approximately 2.5 milliseconds. The pressure–time response plot recorded by piezoelectric PCB transducers using a digital storage oscilloscope is shown in Fig. 2. The incident Mach number was measured using two PCB pressure transducers, and condition 5 of the shock tube was estimated using a one-dimensional gas dynamics calculator based on Rankine–Hugoniot relationships.[45] Air was employed as the test gas. The initial conditions of pressure and temperature in the driver and driven tubes were used as inputs for the calculations. The estimated pressure and temperature of condition 5 were about 0.59 MPa and 520 K, respectively, for the Mach number 1.5.[46] To assess the effects of shock wave exposure, CdS samples were analyzed before and after shock wave treatment using various characterization techniques, including powder X-ray diffraction (XRD), Raman spectroscopy, UV-Vis Diffuse Reflectance Spectroscopy (DRS), Photoluminescence (PL) spectroscopy, and Field-Emission Scanning Electron Microscopy (FE-SEM).
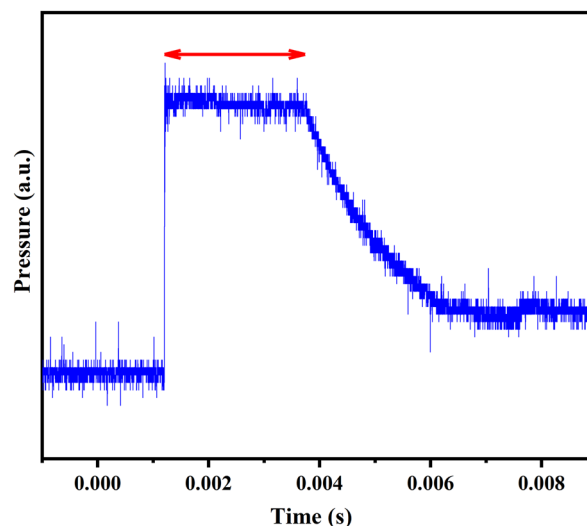

Fig. 2 Time response recorded by piezoelectric PCB transducers using a digital storage oscilloscope.

Characterization technique details

The XRD patterns of CdS before and after shock-loaded conditions were recorded using a Bruker D2 Phaser X-ray powder diffractometer equipped with a CuKα1 radiation source (λ = 1.5406 Å). Data collection was performed over a 2θ range of 20° to 80° with a step size of 0.02°. XRD analysis was employed to investigate the structural characteristics of CdS before and after shock wave treatment and to identify any phase transformations induced by the shock wave exposure. The diffraction patterns were refined using FullProf software, incorporating one structural model: the hexagonal structure ($P6_3mc$ space group, ICSD #: 043599).

Raman spectra of CdS before and after shock-loaded conditions were obtained using a Renishaw confocal Raman microscope with a 532 nm (50 mW) laser source. The system had an axial resolution of less than 1 μm and a lateral resolution of 0.5 nm. Spectral data were recorded within the 100–1000 cm^{-1} range to analyze vibrational modes and structural modifications caused by shock wave treatment.

UV-Vis DRS of CdS before and after shock-loaded conditions was carried out using a SHIMADZU UV-5600 PLUS UV-Vis NIR spectrophotometer, which operates across a broad wavelength range of 185–3300 nm. For this analysis, spectral data were recorded between 200 and 800 cm^{-1} to evaluate changes in the optical properties of CdS following shock wave exposure.

PL spectra of CdS before and after shock-loaded conditions were measured using a Perkin Elmer PL 6500 spectrometer, covering a wavelength range of 190–900 nm. The instrument featured an accuracy of 0.5 nm, a reproducibility of 0.2 nm, and a spectral resolution of 1 nm. Measurements were conducted in real time with a high scanning speed of up to 24 000 nm min^{-1}. The spectra, recorded between 300 and 700 nm with an excitation wavelength of 395 nm, provided insights into atomic defects and their impact on the optical properties of CdS.

FE-SEM of CdS before and after the shock-loaded condition was performed using a SIGMA HV – Carl Zeiss system equipped with a Bruker Quantax 200 – Z10 EDS detector. The instrument was operated at an accelerating voltage range of 200 V to 30 kV, offering magnifications from 20× to 1 000 000×. It provides resolutions of 1.0 nm at 30 kV and 3 nm at 1 kV, with the maximum probe current exceeding 100 nA. The 2D surface profile was generated using MountainsLab software. FESEM analysis was conducted to examine morphological variations and elemental composition, identifying structural changes resulting from shock wave exposure.

Results and discussion

Powder X-ray diffraction (XRD)

Fig. 3 illustrates the (a) XRD pattern of CdS with a standard pattern and (b) the hexagonal structure of CdS along the *c*-axis. The obtained diffraction peaks align with the JCPDS card no.
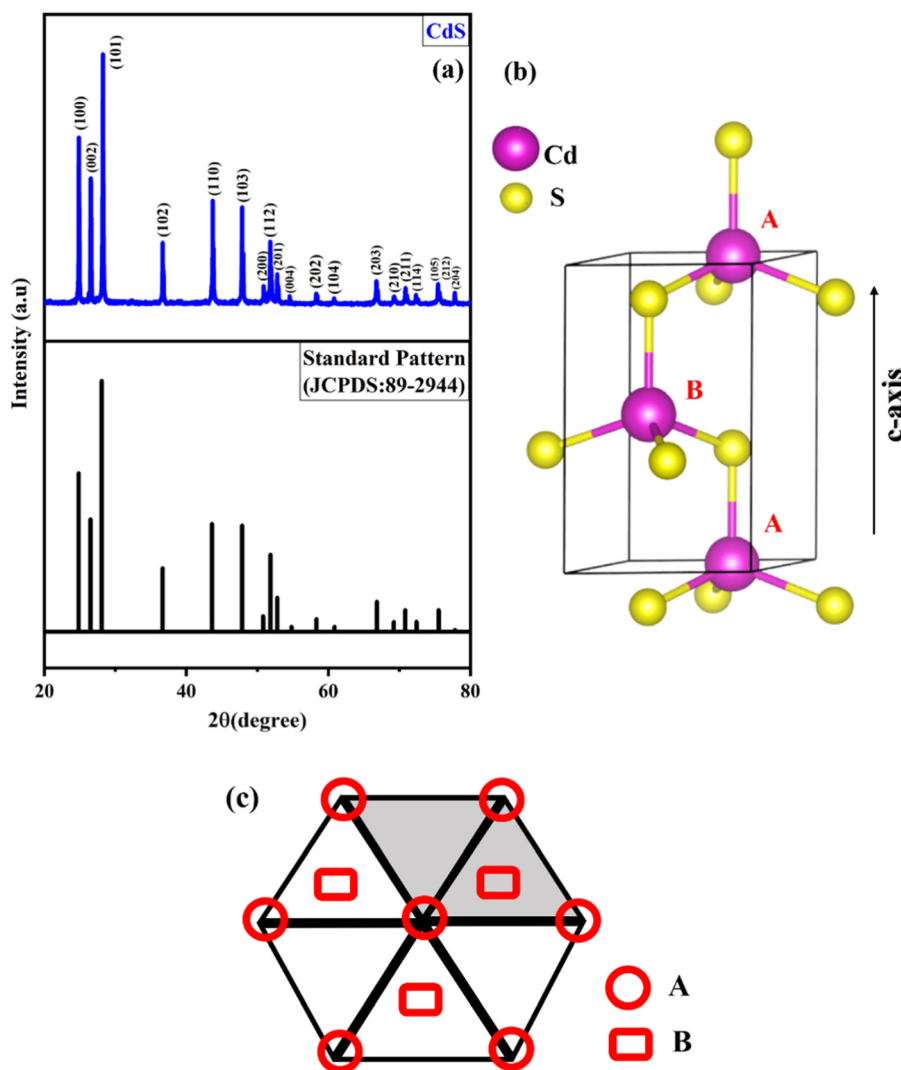

Fig. 3 XRD pattern and structure: (a) XRD pattern of CdS with a standard pattern. (b) Hexagonal structure of CdS along the *c*-axis. (c) Top-view of CdS in the hexagonal structure.

89-2944, confirming its crystallographic identity. The material crystallizes in a hexagonal structure with a $P6_3mc$ space group, characterized by mirror and glide plane symmetry, ensuring structural consistency. Cd and S atoms form a wurtzite-type arrangement, which is a common structure in II–VI semiconductors. Each Cd atom is tetrahedrally coordinated with four S atoms, and each S atom is coordinated with four Cd atoms, forming a stable covalent network stacked along the c-axis with weak van der Waals forces. This arrangement leads to a repeating hexagonal lattice following an ABABAB-type stacking sequence. Fig. 3(c) shows a top view of CdS in a hexagonal structure. Their corresponding lattice parameters are $a = b = 4.14$ Å, $c = 6.71$ Å, and the unit cell volume is 99.67 Å^3. This stacking sequence ensures uniformity in atomic positioning and contributes to the material's overall stability. The observed crystal structure is well-matched with previous reports.[47,48]

Fig. 4(a) shows the XRD pattern of CdS before and after shock-loaded conditions. After CdS subjected to 100, 200, 300, and 400 shock pulses showed no new peaks or peak disappearance. This indicates that its crystal structure remains unchanged. The material retains its hexagonal phase even under repeated shock exposure. Structural stability is maintained up to 400 shock pulses. But minor peak shifts towards a lower angle were observed in the (100), (002), and (101) planes for 100, 200, and 300 shock pulses. Fig. 4(b) shows the zoomed version of

(100), (002), and (101) planes. Shock waves induce rapid compression, leading to deformation in the crystal lattice, which leads to either lattice relaxation or rapid expansion, depending on the material's response to extreme conditions. This process can alter the internal arrangement of atoms, influencing structural stability.[49,50] Additionally, the presence of uniform tensile strain at right angles introduces further distortions in the lattice, which affects atomic spacing and induces mechanical stress. As a result, the interplanar spacing (d-spacing) alters, disrupting the equilibrium structure. This increase in d-spacing directly impacts XRD patterns, causing diffraction lines to shift toward lower diffraction angles. Such shifts provide valuable insights into strain-induced lattice modifications and the extent of deformation under shock wave exposure.[51] The lower-angle shift in diffraction lines, caused by tensile strain and increased d-spacing, is reverted at 400 shock pulses due to structural recovery. At a further 400 shock pulses, the material undergoes lattice rearrangement, where the accumulated strain is gradually released. This relaxation can result from restoring the interplanar spacing to its original value. As a result, the diffraction lines shift back to their initial positions, indicating that the material regains its original lattice configuration despite previous deformation.

Fig. 5 shows Rietveld's refinement of CdS before and after the shock-loaded condition. The analysis confirmed that CdS maintained its structural stability. No phase transition or peak disappearance was observed. Stability was retained even after
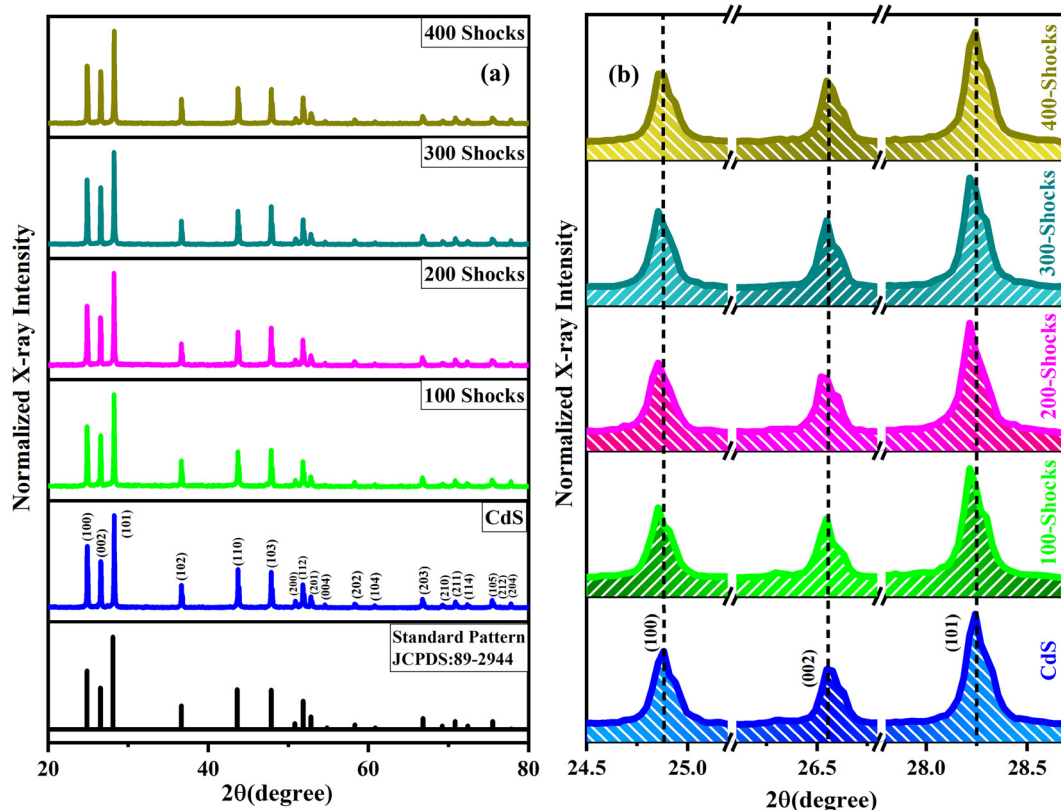

Fig. 4 XRD patterns: (a) CdS before and after the shock-loaded condition. (b) Zoomed version of (100), (002), and (101) planes.
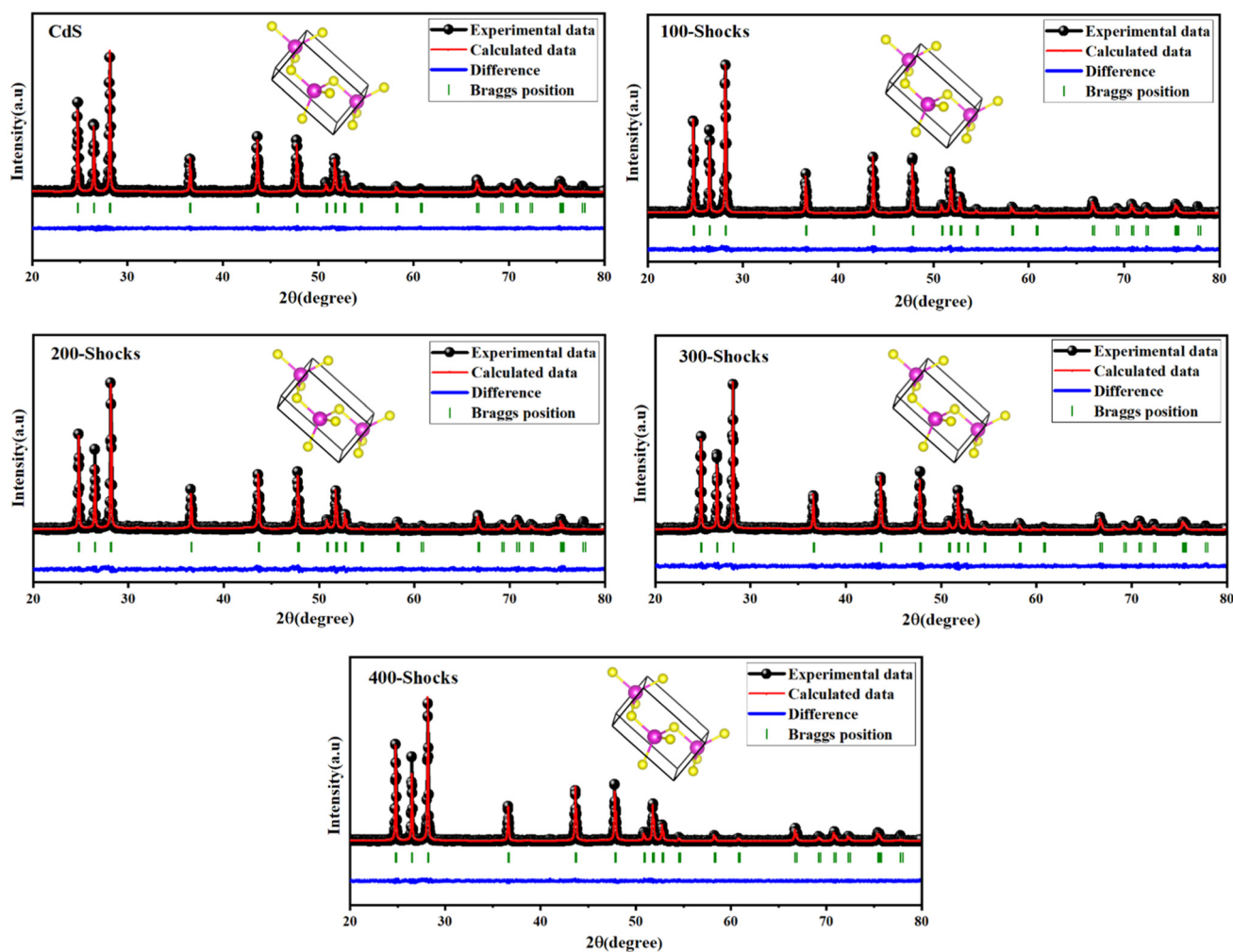
Fig. 5 Rietveld's refinement of CdS before and after the shock-loaded condition.

400 shock pulses, as confirmed through Rietveld's refinement. The calculated lattice parameters and unit cell volume, presented in Table 1, exhibit fluctuations under shock wave-loaded conditions. At 100, 200, and 300 shock pulses, the lattice parameters (a, b, and c) and unit cell volume (V) decreased due to lattice contraction.[52] This contraction induced lattice distortion, leading to a peak shift in the diffraction pattern. At 400 shock pulses, the lattice parameters increased due to shock wave-induced expansion,[53] restoring the distorted lattice. Consequently, the previously shifted peaks returned to their original positions. The direct proportionality between the lattice parameters and unit cell volume highlights the structural response to shock pulses. The interplay between contraction and expansion reflects the dynamic structural modifications under shock wave exposure. The trend of lattice parameter and unit cell volume variation with shock pulses is depicted in Fig. 6, providing insights into the material's structural adaptability.

The average crystallite sizes of CdS were calculated using the Debye–Scherrer formula, $D = \dfrac{K\lambda}{\beta \cos\theta}$[54] for before and after shock-loaded condition. Dislocation density values were calculated using the following equation, $\delta = \dfrac{1}{D^2}$.[55] The lattice strain (ε) values were calculated using the equation; $\varepsilon = \beta/4 \times \tan\theta$.[56] The average crystallite size of CdS before subjecting it to shock waves was found to be 24 nm; after shock wave exposure, a fluctuation in average crystallite size was observed. For 100 shock-loaded conditions, the crystallite size was reduced to 21 nm, and for 200 shock pulses, it was reduced to

Table 1 Lattice parameters of CdS before and after the shock-loaded condition

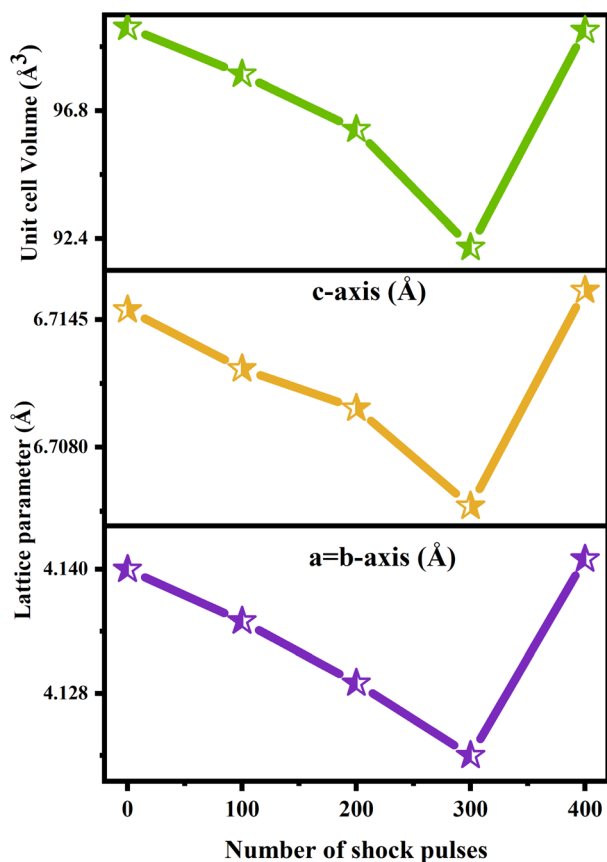| Number of shock pulses	Structure	Space group	Lattice constant $a = b, c$ (Å)	Unit cell volume (Å³)	GoF
0	Hexagonal	$P6_3mc$	4.140, 6.715	99.67	1.3
100	Hexagonal	$P6_3mc$	4.135, 6.712	98.06	1.3
200	Hexagonal	$P6_3mc$	4.129, 6.710	96.16	1.4
300	Hexagonal	$P6_3mc$	4.122, 6.705	92.10	1.1
400	Hexagonal	$P6_3mc$	4.141, 6.716	99.57	1.5

Fig. 6 Variation plot of lattice parameters and unit cell volume against the number of shock pulses.

20 nm. A continued decrement was noted at 300 shock pulses, reaching 19 nm. However, beyond this point, a reversal in the trend was observed. At 400 shock pulses, the crystallite size increased to 23 nm. The variation in average crystallite sizes was observed due to shock wave induced dynamic recrystallization. The high strain rates and localized heating generated during shock-wave exposure facilitate grain refinement. These conditions cause a recrystallization process, altering the crystallite structure. As the material undergoes repeated shock loading, changes in crystallite size become evident. Initially, grain refinement dominates, reducing crystallite size. However, at higher shock pulses, recovery mechanisms may lead to an increase in size.[57] Dislocation density and lattice strain are key indicators for understanding crystal defects and overall crystallinity, with their variations closely linked to changes in crystallite size. At 100, 200, and 300 shock pulses, a progressive decrease in crystallite size was observed, leading to an increase in both dislocation density and lattice strain. This trend arises due to the higher density of grain boundaries in smaller crystallites, which act as defect sites and lead to increased lattice distortions. As grain boundaries accumulate, internal stress within the material rises, resulting in elevated strain. The increased dislocation density further indicates a greater concentration of defects, disrupting the atomic

arrangement within the crystalline planes. The rise in lattice strain suggests that the material experiences increased internal energy, making it more prone to deformation under external stress.[58] However, at 400 shock pulses, a reversal in this trend occurred, with crystallite size increasing and both dislocation density and lattice strain decreasing. The growth in crystallite size reduces the number of grain boundaries, minimizing structural imperfections. With fewer defect sites, the material exhibits lower dislocation density, reflecting a more stable atomic arrangement. The reduction in lattice strain indicates decreased internal stresses, leading to improved structural stability. This change may be influenced by dynamic recrystallization, where shock wave exposure promotes atomic rearrangement and defect recovery, facilitating grain coalescence and reducing distortions within the lattice.[59] Compression may occur more easily along the elongated c-axis as shock pulses propagate through the sample.[60,61] Due to anisotropic behavior, it is significantly easier to compress the material along the elongated c-axis than along the ab-plane, primarily due to differences in bonding and structural arrangements. CdS, being an anisotropic material, exhibits strong covalent bonding within the ab-plane, while the layers are held together along the c-axis by weak van der Waals forces. Under shock wave-loaded conditions, these weaker interlayer forces are more easily overcome, making the c-axis more susceptible to compression. This is because the elastic modulus, a measure of stiffness, is typically lower along the c-axis, offering less resistance to deformation compared to the more rigid ab-plane.[62] Due to such effects, XRD patterns typically show shifts of the diffraction peaks toward higher 2θ angles by reduced d-spacing, peak broadening from strain, or intensity changes due to lattice distortion. However, in this study, no such changes were observed up to 400 shock pulses. This absence of variation in the peak position, width, or intensity suggests that the CdS lattice retains its structural integrity under the shock-loaded conditions. Additionally, materials with larger crystallite sizes typically exhibit better thermal stability under extreme conditions, emphasizing the importance of crystallite size in maintaining material stability. A reduced density of grain boundaries lowers defect formation, preventing rapid degradation and enhancing the material's resilience under extreme conditions.[63] These observations highlight the intricate relationship between crystallite size, lattice strain, and dislocation density under shock wave treatment. While the initial reduction in crystallite size increases defect concentration and strain, at 400 shock pulses, it promotes structural recovery, leading to improved crystallinity and stability. Overall, these findings confirm the excellent structural stability of CdS under shock-loaded conditions. Maintaining the structural stability of the material is essential, as it directly influences the material's reliability and performance in demanding applications such as energy storage and aerospace systems. Fig. 7 shows the variation plot of crystallite size *versus* lattice strain and dislocation density against the number of shock pulses.
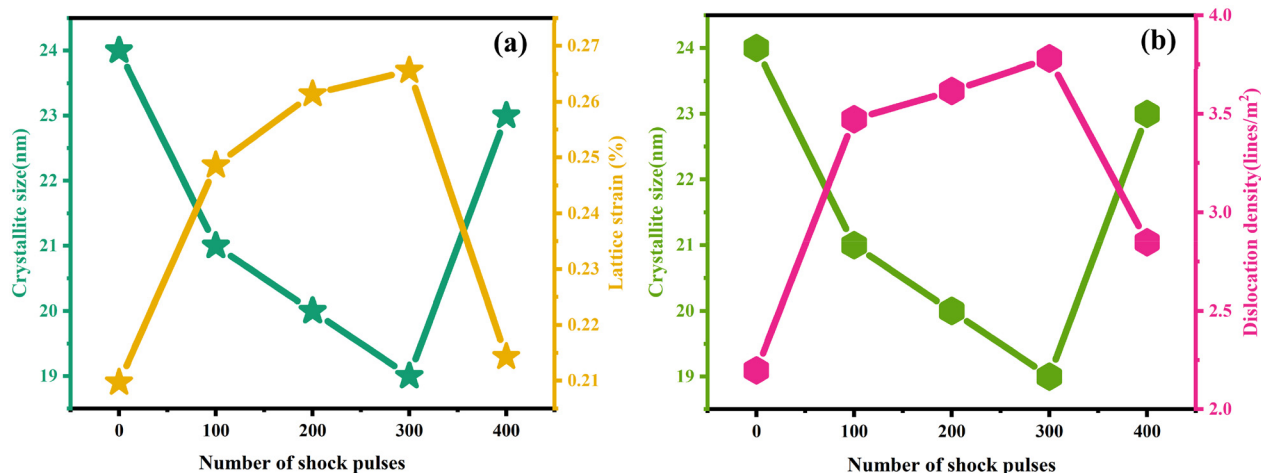
Fig. 7 Variation plot of crystallite size *versus* (a) lattice strain and (b) dislocation density against the number of shock pulses.

Raman spectroscopy

Fig. 8 shows the Raman spectra of CdS before and after shock-loaded conditions and zoomed version of the 1LO and 2LO peaks. The present study observed three optical vibrational Raman-active modes at 301, 602, and 904 cm^{-1}. The 301 cm^{-1} peak was assigned to the fundamental longitudinal optical (1LO) phonon mode. In comparison, the 602 cm^{-1} peak corresponded to the first overtone longitudinal optical (2LO)

phonon mode, and the 904 cm^{-1} peak was identified as the second overtone longitudinal optical (3LO) phonon mode. These assignments are well aligned with previous reports.[64] Upon exposure to shock waves, no appearance or disappearance of Raman peaks was observed, indicating that the fundamental vibrational modes remained intact. However, a slight peak shift was detected from 100 to 300 shock pulses, where a minor blueshift was observed in the Raman spectrum. This effect is primarily attributed to shock wave-induced rapid
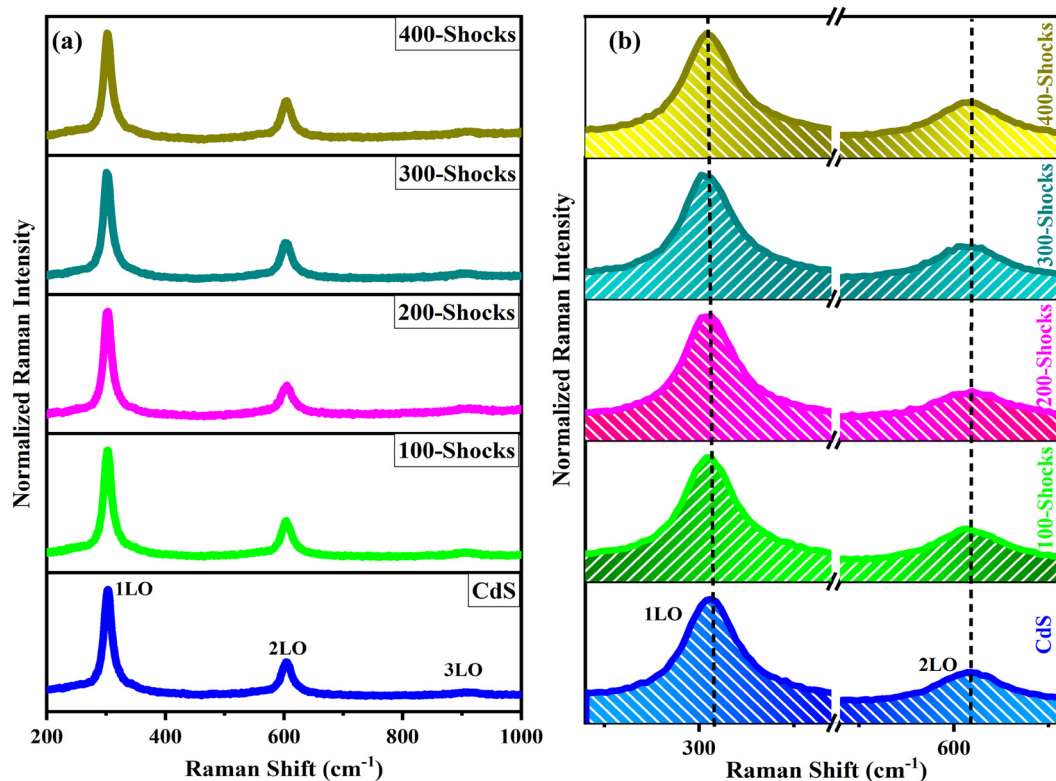

Fig. 8 Raman spectra of CdS before and after the shock-loaded condition. (a) Range: 200–100 cm^{-1}. (b) Zoomed version of 1LO and 2LO peaks.

lattice compression, wherein the rapid impact of shock waves reduces atomic spacing, thereby strengthening interatomic bonds and increasing vibrational energy. Rietveld refinement revealed lattice compression and reduced atomic spacing, as evidenced by decreased lattice parameters and unit cell volume. The observed blueshift can also be attributed to an increase in dislocation density at 300 shock pulses. These dislocations generate localized compressive strain fields within the lattice, which elevate phonon frequencies and contribute to the peak shift. Additionally, the reduction in crystallite size enhances phonon confinement effects, further supporting the observed blueshift. Additionally, bond stiffening under high-pressure conditions further raises phonon frequencies. In some cases, defect reduction through shock-induced annealing can restore lattice order, enhance phonon confinement, and contribute to the observed blueshift.[65,66] At 400 shock pulses, the shifted peak reverted to its original position, indicating a redshift in the Raman spectrum. A redshift occurs when bonds weaken due to thermal effects, increasing bond lengths and lowering vibrational frequencies. The recovery of the peak position suggests that as the material experienced thermal energy accumulation led to partial structural relaxation, counteracting the initial compression effects.[67,68] Lattice expansion induced by shock waves led to increased bond lengths, as confirmed by larger lattice parameters and unit cell volume obtained through Rietveld refinement at 400 shock pulses. The resulting redshift can be attributed to a reduction in dislocation density, which alleviates residual strain within the crystal lattice. Furthermore, the decrease in crystallite size weakens phonon confinement effects, thereby contributing to the observed redshift. This behavior highlights that an acoustic shock wave can induce both lattice compression (leading to a blueshift) and thermal expansion or bond weakening (resulting in a redshift), with the observed Raman shifts reflecting a complex interplay between dislocation density, crystallite size, lattice strain, lattice parameters, and unit cell volume. No new peaks were detected, which further suggests that no significant structural phase transition occurred, reinforcing the material's resilience under shock loading conditions.

UV-Vis diffuse reflectance spectroscopy (DRS)

The CdS before and after shock-loaded reflectance spectra are shown in Fig. 9. After the shock-loaded condition, the optical properties of CdS were modified, indicating changes in light absorption and reflection. To analyze these effects, the bandgap was calculated for CdS before and after the shock-loaded condition. The Kubelka–Munk equation was employed to determine the bandgap values, providing insights into the material's optical transitions. These calculations help in understanding how shock loading influences the optical behavior of CdS before and after the shock-loaded condition. The Kubelka–Munk equation is applied to the reflectance data to calculate the optical bandgap of CdS under shock-loaded conditions. This method will convert diffuse reflectance into absorption-like values.
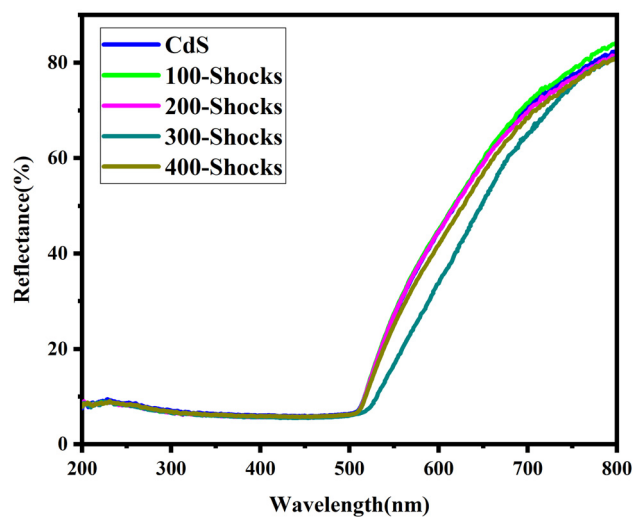

Fig. 9 Reflectance spectra of CdS before and after the shock-loaded condition.

Reflectance is correlated with absorption, allowing the optical bandgap to be estimated based on the material's optical transitions. This relationship provides insight into how the material interacts with light. By linking reflectance to absorption properties, the bandgap can be accurately determined. The band gap was calculated using the following equation $(F(R)h\upsilon)^2 = A(h\upsilon - E_g)$, where $F(R_\infty)$ stands for Kubelka–Munk function, and can also be called the remission function, and R_∞ refers to diffuse reflectance, which is obtained from $R_\infty = R_{sample}/R_{standard}$. A refers to a constant given by the transition probability and the diffuse reflectance R_∞, $h\upsilon$ represents incident photon energy, and E_g is denoted as the bandgap.[69] Fig. 10 illustrates the Kubelka–Munk plot. The plot is drawn between $(F(R_\infty)h\upsilon)^2$ and $h\upsilon$, where straight lines are fitted to match the experimental bandgap curves. These lines help in identifying the optical transition behavior of CdS. To determine the optical bandgap, the fitted lines are extended until they intersect the $h\upsilon$ axis. This intersection point represents the bandgap energy of the material. Such an approach ensures an accurate estimation of the optical bandgap.

Initially, CdS exhibited a bandgap of 2.37 eV, which was well matched with the values reported in the literature for CdS in a hexagonal structure.[70] After shock wave exposure, a reduction in the bandgap was observed at 100 shock pulses, the bandgap was slightly reduced to 2.36 eV, followed by a further decrease in the bandgap to 2.35 eV at 200 shock pulses. A significant drop was observed after 300 shock pulses, where the bandgap reached 2.24 eV, aligning well with reported values for hexagonal CdS.[71] This reduction suggests a notable alteration in the material's optical properties. Under shock wave exposure, the material experiences rapid compression, which can cause contraction or expansion of the crystal lattice, and leads to alternation in the crystal lattice. This induces lattice deformation, causing atoms to shift from their original positions. The result-
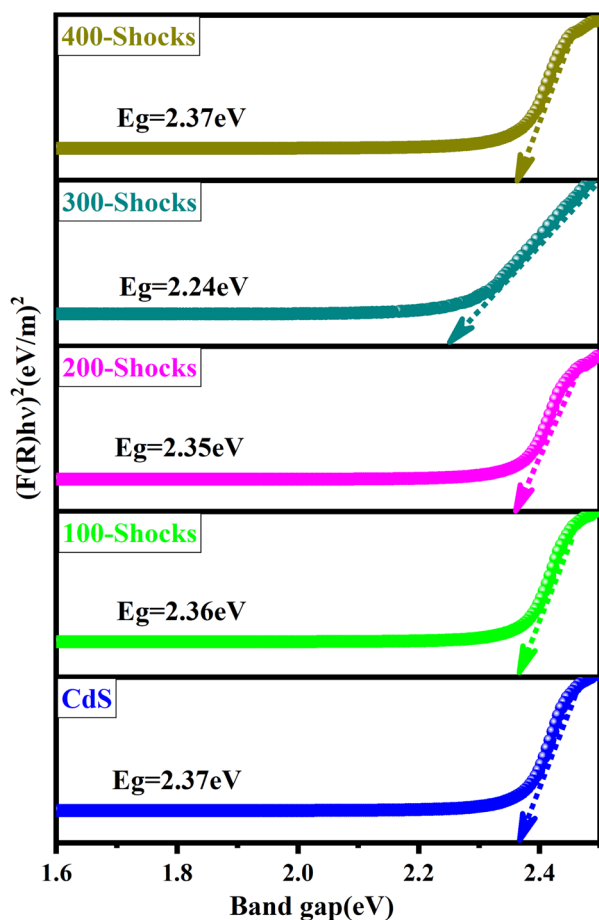
Fig. 10 Kubelka–Munk plot of CdS before and after the shock-loaded condition.

ing structural distortion affects electronic properties, including bandgap modifications.[72] When the crystal lattice contracts, atoms move closer together, which reduces the lattice parameters and increases orbital overlap.[73,74] Such a type of stronger interaction between electronic orbitals lowers the conduction band (CB) and raises the valence band (VB) upwards, resulting in reduced energy requirement for electron excitation

and leading to bandgap narrowing. Structural distortions and lattice defects such as increased lattice strain at 100, 200, and 300 shock pulses introduce localized states near the band edges, forming band tails that extend into the bandgap. These tails enable absorption of lower-energy photons, altering the material's optical properties. Additionally, deep-level defects can lead to mid-band state creation between the CB and VB. These states can act as charge traps, potentially extending carrier lifetimes but also increasing localized energy losses and leading to a lower bandgap.[75] Interestingly, at 400 shock pulses, the bandgap returned to its original value of 2.37 eV. In contrast, shock wave-induced lattice expansion increases the atomic spacing, and causes an increase in lattice parameters, reducing the orbital overlap and weakening electronic interactions. As a result, the conduction band (CB) and valence band (VB) shift in energy, increasing the gap between them and requiring more energy for electronic transitions.[76] Additionally, shock wave-induced thermal energy will anneal out the localized defect states and reduce structural disorder, which leads to reduced lattice strain at 400 shock pulses. It can promote atomic rearrangement, allowing defects to recombine or migrate out of the forbidden energy region. This process reduces band tail states, which are typically caused by structural irregularities near the band edges, and eliminates mid-band states that arise from deep-level defects.[77] As these defect states diminish, the material exhibits a more ordered electronic structure with an increased bandgap at 400 shock pulses. Fig. 11 illustrates the mechanism of bandgap modification of CdS before and after shock-loaded conditions. This reversible bandgap suggests that the material undergoes a reversible change under shock wave exposure. The observed variations in bandgap reflect the influence of shock waves on the electronic structure of CdS.

Photoluminescence (PL) spectroscopy

Fig. 12 presents the PL spectra of CdS before and after shock-loaded conditions in the range of 300–700 nm. The emission peak for CdS before the shock-loaded condition was observed at 518 nm, closely matching previously reported values in the
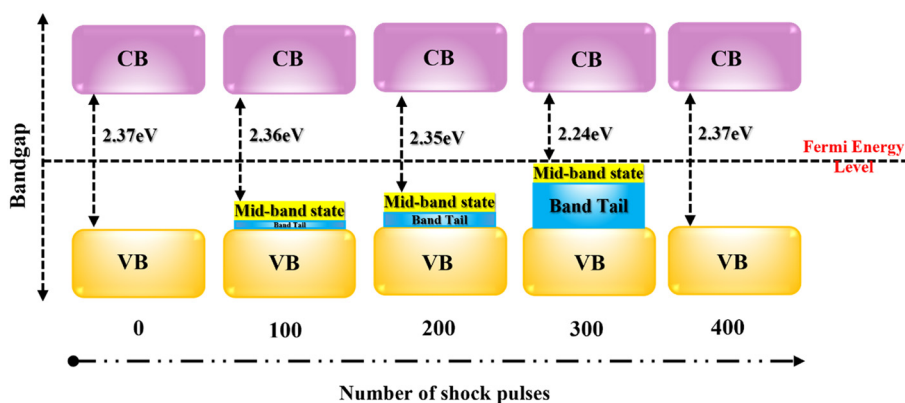

Fig. 11 Mechanism of bandgap modification of CdS before and after the shock-loaded condition.
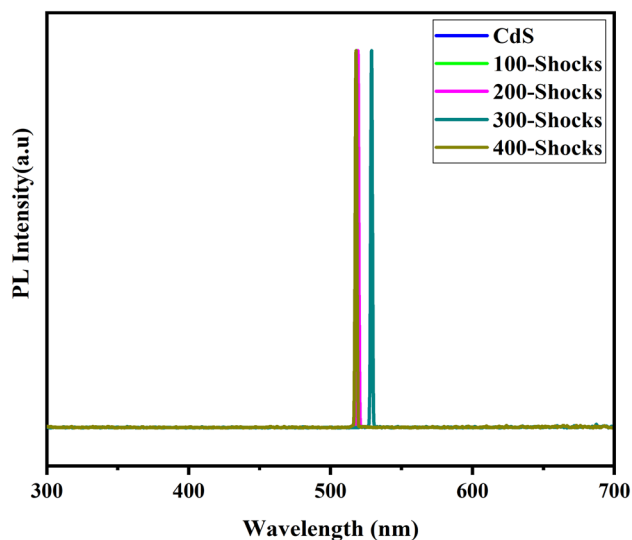
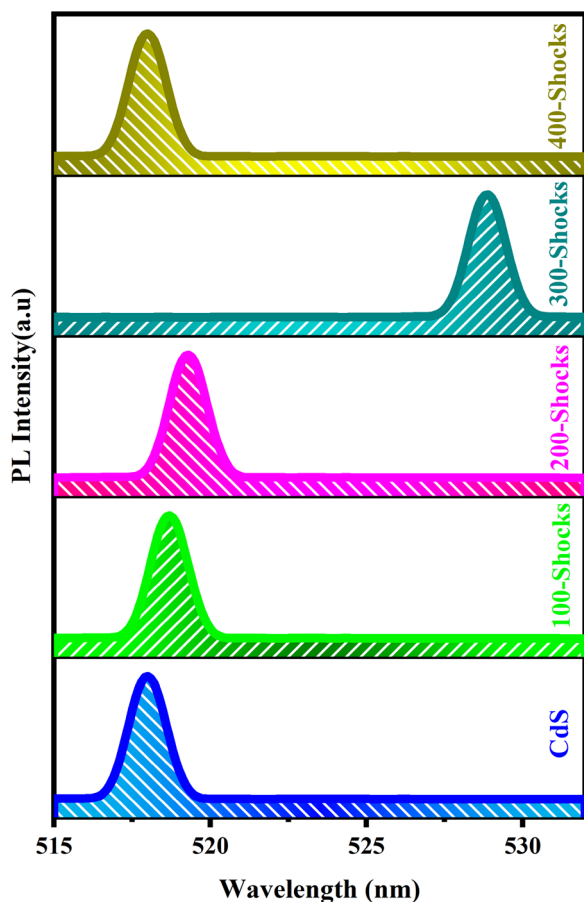**Fig. 12** PL spectra of CdS before and after the shock-loaded condition.

Fig. 13 Zoomed version of the emission peak.

literature.[78] Fig. 13 shows the zoomed version of the emission peak. A slight shift in the emission peak was observed under shock-loaded conditions, with a minor shift appearing at 100

and 200 shock pulses, and more pronounced red shifts to 528 nm were observed at 300 shock pulses. It is well aligned with the literature value for the CdS hexagonal structure, achieved through varying calcination temperatures.[79]

Under shock-loaded conditions, the electronic structure undergoes significant modifications, leading to a redshift in the PL emission peak. When a shock wave propagates through a material, it causes lattice contraction by reducing the spacing between atoms, which enhances orbital overlap. This distortion introduces localized shallow traps and mid-gap states within the bandgap and the energy levels that arise due to structural disorder and strain. These straps effectively lower the energy required for electronic transitions, allowing charge carriers to undergo recombination at lower energy levels. Instead of radiating energy as photons, a significant portion is dissipated through phonon interactions, which results in non-radiative recombination.[80–84] However, at 400 shock pulses, the removal of shallow trap states can lead to a reversal of these effects, allowing the emission peak to shift back toward its original position and shift toward a lower wavelength, which is a blueshift. Consequently, the PL emission peak shifts to a longer wavelength, causing a redshift in the spectrum. Conversely, a blueshift in PL occurs when the shock-induced strain enhances charge carrier mobility, particularly for excitonic electron–hole pairs. As the material undergoes lattice expansion, the mobility of these carriers improves, reducing their likelihood of being trapped in localized defect states. This increased mobility facilitates efficient exciton recombination, weakening the influence of shallow traps and mid-gaps. As a result, the binding energy of these straps decreases, leading to their delocalization. With fewer low-energy recombination pathways, the emission peak shifts toward shorter wavelengths, producing a blueshift in the PL spectrum.[85,86] Fig. 14 shows the mechanism of the emission peak shift. Fig. 15 illustrates the CIE chromaticity diagram of CdS before and after the shock-loaded condition. The y-values (0.708) consistently exceeded the x-values (0.243), indicating that an emission peak corresponds to green emission, which originates from electron transitions between the conduction band and an acceptor level. This shift indicates subtle modifications in the electronic structure, likely influenced by external factors such as shock loading. Despite this variation, the optical characteristics remain stable, maintaining consistency with prior studies. Such emission behavior highlights the material's potential for optoelectronic applications, particularly in photonic devices.[87,88] For CdS before and after shock-loaded conditions, the green color purity was 71.59%. After 100, 200, and 300 shock pulses, the color purity increased to 72.12%, 72.31%, and 81.09%, respectively. However, after 400 shock pulses, the emission peak returned to its original position, and the color purity reverted to 71.59%. High color purity is crucial in solid-state lighting devices as it ensures high-quality color rendering and efficiency. Improved color purity allows for more precise and vibrant lighting, enhancing the performance and application potential of solid-state lighting technologies, such as LEDs.[89]
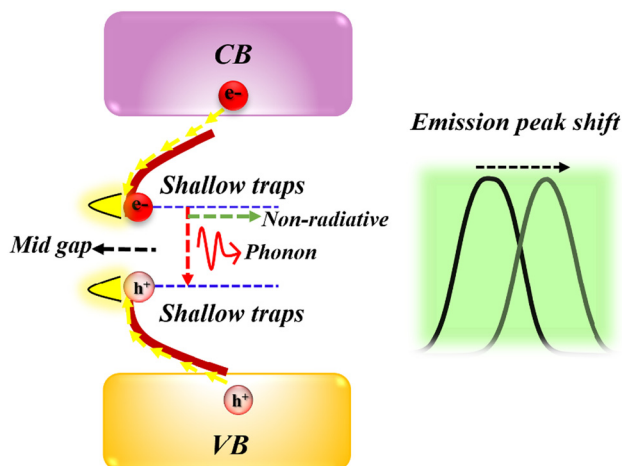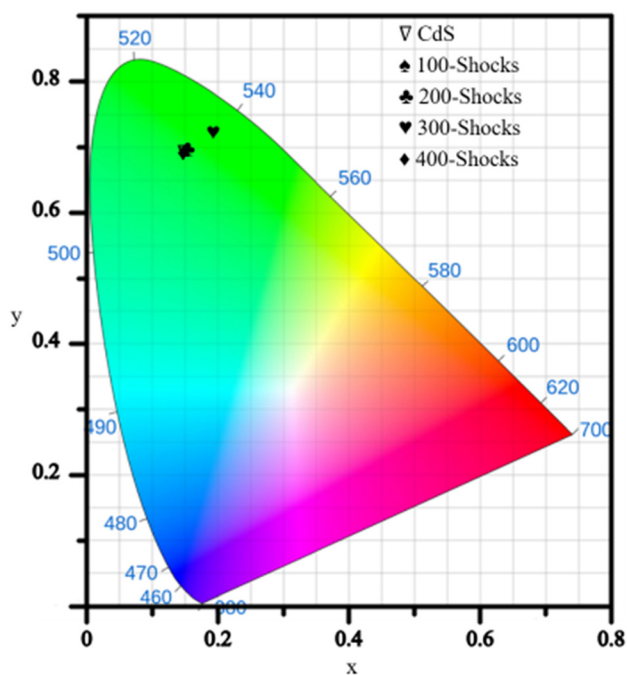
Fig. 14 Mechanism of the emission peak shift.

Fig. 16 EDX spectrum of CdS.

Fig. 15 CIE (*x, y*) chromaticity diagram of CdS before and after the shock-loaded condition.

Field emission scanning electron microscopy (FE-SEM)

Fig. 16 presents the EDX spectrum of CdS. The EDX spectrum confirms the presence of cadmium (Cd) and sulfur (S) atoms. Fig. 17 and 18 present the FE-SEM images of CdS before and after shock loading, with a scale bar of 100 nm and 200 nm, accompanied by corresponding 2D surface profiles. Initially, CdS exhibits a rod-like morphology, which is characteristic of its anisotropic crystal growth. Anisotropic crystal growth refers to the non-uniform expansion of a crystal structure along different crystallographic directions, leading to distinct shapes and morphologies due to different surface energies. For example, hexag-
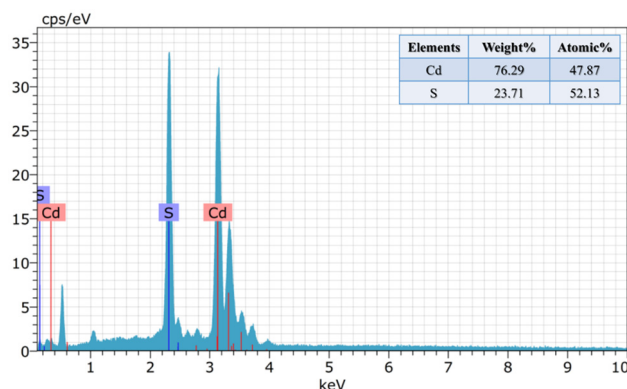
onal and tetragonal structures tend to grow anisotropically due to differing surface energies. This growth behavior influences material properties, making it essential for applications in semiconductors, nanomaterials, and optoelectronics.[90] For 100 and 200 shock pulses, the rod-like morphology remains the same. Once the shock pulses increased to 300, the rod-like morphology changed to a cube-like morphology due to shock wave-induced dynamic recrystallization.[91] A hexagonal crystal structure of CdS can also exhibit a cube-like morphology.[92]

Acoustic shock waves significantly influence the morphology of the sample due to its low thermal transport values. CdS has a low thermal conductivity of 2.9 W m^{-1} K^{-1}, which allows thermal energy to accumulate and trigger the recrystallization process and turn the material into a molten state. For 100 shock pulses, the energy input is insufficient to change the morphology. At 200 shock pulses, localized heating becomes more pronounced, and the onset of melting begins to appear. This early-stage melting initiates morphological evolution, although it remains below the threshold required for dynamic recrystallization or complete morphology transition. As the number of shock pulses increases to 300, the energy reaches a critical threshold. The rapid deposition of energy, combined with the material's poor ability to dissipate heat due to low thermal conductivity, results in intense localized heating that induces dynamic recrystallization and leads to a molten state. Consequently, the rod-shaped particles undergo fragmentation and reorganization, gradually transforming into a cube-like morphology. This transformation is primarily driven by the thermal softening, fragmentation, and rapid resolidification induced by the shock pulse, where a combined transient pressure of 0.59 MPa and a transient temperature of 520 K generate a superheating and supercooling effect within milliseconds. The rapid heating initiates a premelting process, wherein the material briefly enters a molten-like state before resolidifying. If the material has low thermal conductivity, this premelting phase and transient molten state can allow morphological changes by promoting localized melting and subsequent cooling.[93]

Due to the low thermal conductivity of CdS, heat is localized rather than dispersed, allowing sufficient thermal energy

Fig. 17 FE-SEM images of CdS before and after shock loaded condition, with a scale bar of 100 nm, accompanied by corresponding 2D surface profiles.

to accumulate at a specific region. These localized molten zones enable the formation of new grain boundaries. Upon rapid cooling, these zones solidify into a more compact, energetically favorable cube morphology. As recrystallization progresses, the particles reorganize and stabilize into a cube-like morphology due to the molten phase solidifying under rapid

shock waves induced by lattice compression. This transformation occurs entirely within the hexagonal crystal structure of CdS, meaning that while the external morphology changes significantly, the fundamental crystallographic arrangement remains unaltered. The cube-like morphology observed at intermediate shock pulses arises as a result of the thermal
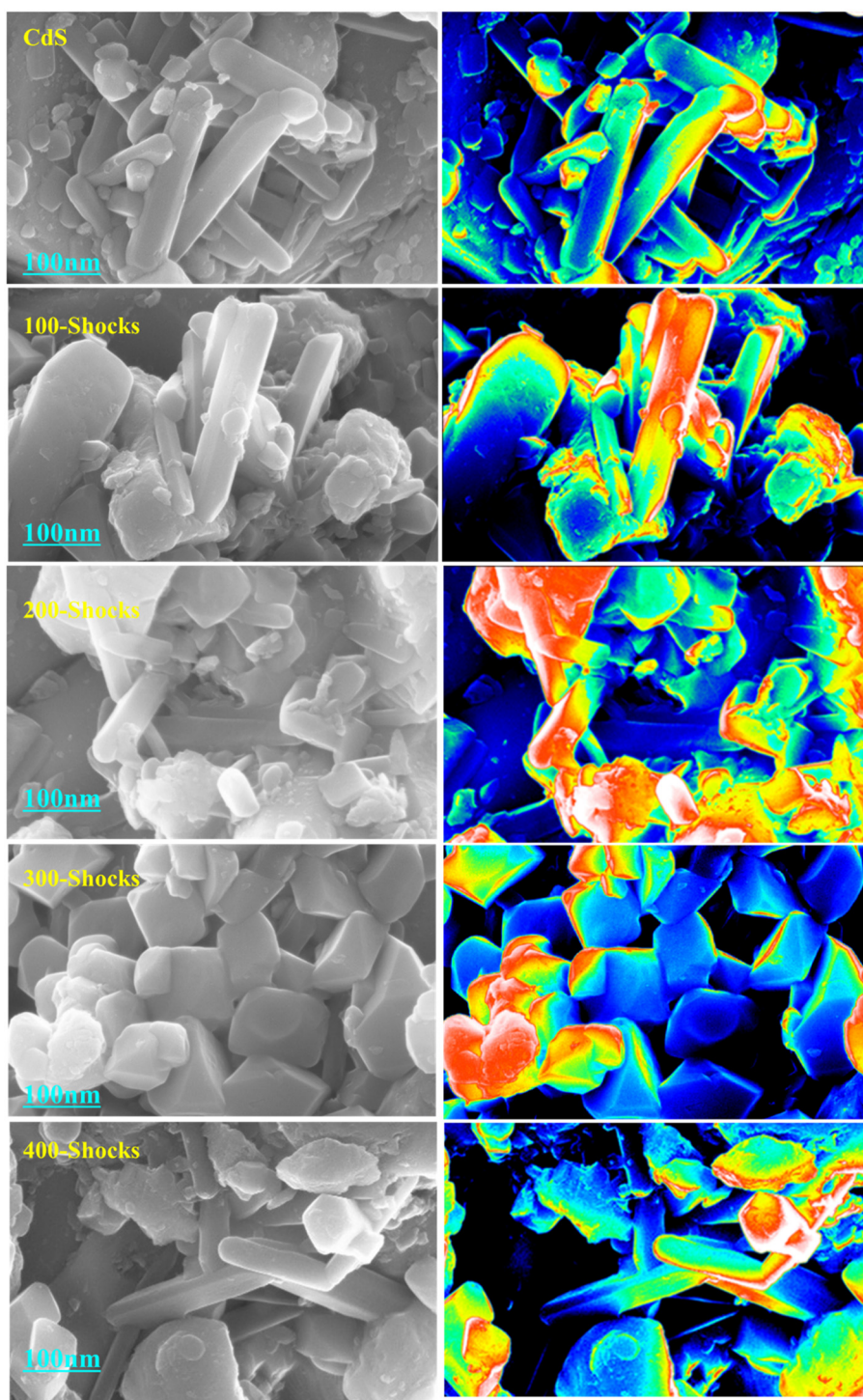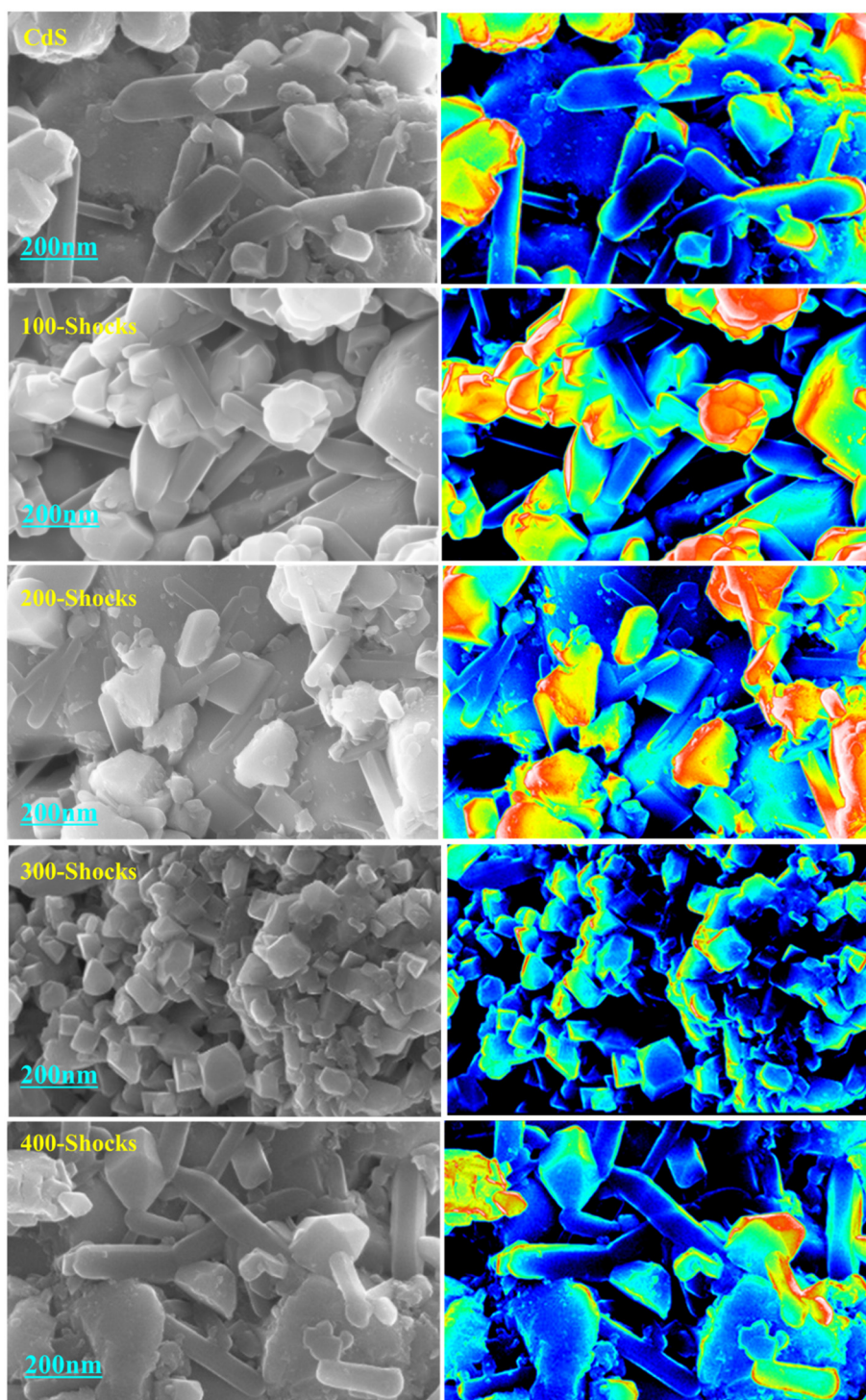
Fig. 18 FE-SEM images of CdS before and after shock loaded condition, with a scale bar of 200 nm, accompanied by corresponding 2D surface profiles.

energy distribution, which facilitates the formation of a more compact morphological change through localized resolidification at 300 shock pulses.

However, as the number of shock pulses reaches 400, the cube-like morphology reverts to a rod-like morphology. This reversal is attributed to thermal relaxation and atomic rearrangement mechanisms that promote the recovery of the material's original elongated shape. The further shock wave exposure allows the thermal energy to dissipate more gradually, encouraging the recrystallization process to favor the rod-like morphology once again. This suggests that the material has an inherent tendency to recover its original shape when

sufficient thermal energy is provided, allowing atomic diffusion and structural realignment to occur. The reversible dynamic recrystallization is driven by the material's lower thermal conductivity, causing heat dissipation to occur gradually. This slow release of heat promotes defect realignment and atomic rearrangement within the crystal lattice. So, at 400 shock pulses, the defect reorganization becomes more extensive, facilitating further atomic stabilization and enabling the crystal lattice to regain its order. This ongoing process, where strain-induced defects are both formed and annealed out under the combined effects of rapid pressure and thermal energy, results in dynamic recrystallization and the restoration of the rod-like morphology. Additionally, the continuous thermal fluctuations enable localized energy redistribution, facilitating preferential growth leading to the reformation of the rod-like morphology. During shock wave experiments, the processes of melting and recrystallization occur within milliseconds, minimizing the likelihood of complete liquefaction. To mitigate contamination and unintended oxidation, the pouch was completely sealed without any gaps, ensuring the sample's integrity and stability throughout the experiment.[94]

Despite these distinct morphological transformations, XRD analysis confirms that no structural phase changes occur, reinforcing that the crystallographic structure integrity of the material remains stable under shock wave exposure. The CdS sample maintains its hexagonal crystal structure throughout the process, demonstrating that while the external morphology dynamically evolves under varying shock conditions, the internal crystal framework remains unchanged. The observed sequence of transformations highlights the intricate balance between fragmentation, recrystallization, and thermal recovery mechanisms, where the interplay of temperature and pressure leads to tuning the morphology without altering the underlying hexagonal phase. It has been previously reported by S. Rajkumar *et al.* that Nd_2O_3 showed morphological changes from irregular particle shapes to a circular hexagon-shaped morphology without any structural changes, but the morphology was not reversible.[95] This study underscores the role of shock wave-induced thermal effects leading to material modifications, emphasizing that morphology can be tuned through controlled shock wave exposure while preserving the fundamental structural stability of the material.

Conclusion

This study provides valuable insights into the structural, optical, and morphological evolution of CdS and its response under acoustic shock-loaded conditions. XRD and Raman analysis confirm that CdS retains its hexagonal structure up to 400 shock pulses, with only a minor peak shift at 300 shock pulses, which reverts to its original position at 400 shock pulses. The structural stability was further validated through Rietveld refinement. Optical analysis reveals that the bandgap decreases from 2.37 eV to 2.24 eV at 300 shock pulses, indicating enhanced electronic transitions. However, at 400 shock pulses, the bandgap reverts to its original value, demonstrating a reversible optical response. PL spectra exhibit a shift in the emission peak from 517 nm to 528 nm at 300 shock pulses, which returns to its initial position at 400 shock pulses, further confirming the reversibility in optical behavior. Most interestingly, the morphological study shows a striking transformation, where rod-like structures transition into a cube morphology at 300 shock pulses, and it reverts to their original rod-like form at 400 shock pulses. Notably, this reversible morphological transition occurs without any detectable structural changes, highlighting the dynamic adaptability of CdS under shock waves. Overall, these findings demonstrate the remarkable reversibility of CdS in structural, optical, and morphological aspects under shock-loaded conditions. The ability of CdS to maintain its hexagonal structure despite transient peak variations, along with the reversible changes in bandgap, PL emission, and morphology, underscores its structural resilience and dynamic adaptability under acoustic shock waves. The reversible optical properties suggest potential for tunable electronic and optoelectronic applications, where controlled bandgap modulation can enhance device performance. Similarly, the reversible morphological transformation from a rod to a cube and back to rod-like structures, without permanent structural alterations, highlights the material's ability to withstand mechanical stress while retaining its intrinsic characteristics. This reversible tuning can improve CdS-based devices like LEDs, photodetectors, and sensors by enhancing performance and durability. It offers a promising approach to developing adaptable, shock-resistant semiconductor materials for advanced applications. Overall, this study provides crucial insights into the reversible tuning of CdS optical and morphological properties *via* acoustic shock wave exposure, governed by shock-induced dynamic recrystallization. Remarkably, these transformations occur without compromising the material's crystallographic phase. The findings establish acoustic shock waves as a powerful, non-destructive tool for modulating material behavior, highlighting dynamic recrystallization as a key mechanism for morphology control. Further exploration of the underlying recrystallization dynamics could enable the development of materials with engineered responses for next-generation functional applications.

Author contributions

F. I. M. B.: methodology, investigation, data curation, writing – original draft, writing and editing. S. O.: formal analysis. P. K.: formal analysis. S. A. M. B. D.: conceptualization, supervision, investigation, writing review and editing. I. K.: formal analysis and funding acquisition. All the authors discussed the results and commented on the manuscript.

Conflicts of interest

The authors declare no conflict of interest regarding the publication of this paper.

Data availability

Data will be made available on request.

Acknowledgements

References

1 J. Mao, W. Xu and S. Seo, Exploring the dual phases of cadmium sulfide: synthesis, properties, and applications of hexagonal wurtzite and cubic zinc blende crystal structures, *J. Mater. Chem. A*, 2024, **12**, 23218–23243.

2 M. C. Baykul and N. Orhan, Band alignment of $Cd_{(1−x)}Zn_xS$ produced by spray pyrolysis method, *Thin Solid Films*, 2010, **518**, 1925–1928.

3 C. Wang, H. Shang, Y. Tao, T. Yuan and G. Zhang, Properties and morphology of CdS compounded TiO_2 visible light photocatalytic nanofilms coated on glass surface, *Sep. Purif. Technol.*, 2003, **32**, 357–362.

4 H. Khallaf, I. O. Oladeji, G. Chai and L. Chow, Optimization of chemical bath deposited CdS thin films using nitrilotriacetic acid as a complexing agent, *Thin Solid Films*, 2008, **516**, 5967–5973.

5 M. C. Schlamp, X. Peng and A. P. Alivisatos, Improved efficiencies in light emitting diodes made with CdSe (CdS) core/shell type nanocrystals and a semiconducting polymer, *J. Appl. Phys.*, 1997, **82**, 5837–5842.

6 A. K. Rath, S. Bhaumik and A. J. Pal, Mn-doped nanocrystals in light-emitting diodes: energy-transfer to obtain electroluminescence quantum dots, *Appl. Phys. Lett.*, 2010, **97**, 113502–113503.

7 D. Jing and L. Guo, A novel method for the preparation of a highly stable and active CdS photocatalyst with a special surface nanostructure, *J. Phys. Chem. B*, 2006, **110**, 11139–11145.

8 S. Shen and L. Guo, Growth of quantum-confined CdS nanoparticles inside Ti-MCM-41 as a visible light photocatalyst, *Mater. Res. Bull.*, 2008, **43**, 437–466.

9 K. G. Kanade, J. Baeg, U. P. Mulik, D. P. Amalnerkar and B. B. Kale, Nano-CdS by polymer-inorganic solid-state reaction: visible light pristine photocatalyst for hydrogen generation, *Mater. Res. Bull.*, 2006, **41**, 2219–2225.

10 T. Wei, C. Huang, B. J. Hansen, Y. F. Lin, L. J. Chen, S. Y. Lu and Z. L. Wang, Large enhancement in photon detection sensitivity via Schottky-gated CdS nanowire nanosensors, *Appl. Phys. Lett.*, 2010, **96**, 013508.

11 C. Cao, C. Hu, W. Shen, S. Wang, Y. Tian and X. Wang, Synthesis and characterization of TiO_2/CdS core–shell nanorod arrays and their photoelectrochemical property, *J. Alloys Compd.*, 2012, **523**, 139–145.

12 S. Biswas, M. F. Hossain and T. Takahashi, Fabrication of Gratzel solar cell with TiO_2/CdS bilayered photoelectrode, *Thin Solid Films*, 2008, **517**, 1284–1288.

13 M. Bruchez, M. Moronne, P. Gin, S. Weiss and A. P. Alivisatos, Semiconductor nanocrystals as fluorescent biological labels, *Science*, 1998, **281**, 2013–2016.

14 T. Kida, G. Guan and A. Yoshida, $LaMnO_3$/CdS nanocomposite: A new photocatalyst for hydrogen production from water under visible light irradiation, *Chem. Phys. Lett.*, 2003, **371**, 563–567.

15 M. F. Kuehnel, D. W. Wakerley, K. L. Orchard and E. Reisner, Photocatalytic formic acid conversion on CdS nanocrystals with controllable selectivity for H_2 or CO, *Angew. Chem., Int. Ed.*, 2015, **54**, 9627–9631.

16 W. T. Yao, S. H. Yu, S. J. Liu, J. P. Chen, X. M. Liu and F. Q. Li, Architectural control syntheses of CdS and CdSe nanoflowers, branched nanowires, and nanotrees via a solvothermal approach and their photocatalytic property, *J. Phys. Chem. B*, 2006, **110**, 11704–11710.

17 J. S. Jang, U. A. Joshi and J. S. Lee, Solvothermal synthesis of CdS nanowires for photocatalytic hydrogen and electricity production, *J. Phys. Chem. C*, 2007, **111**, 13280–13287.

18 M. Matsumura, S. Furukawa, Y. Saho and H. Tsubomura, Cadmium sulfide photocatalyzed hydrogen production from aqueous sulfite solutions: Effect of crystal structure and preparation method of the catalyst, *J. Phys. Chem.*, 1985, **89**, 1327–1329.

19 Y. Gao, D. Kong, J. Han, W. Zhou, Y. Gao, T. Wang and G. Lu, Cadmium sulfide *in situ* derived heterostructure hybrids with tunable component ratio for highly sensitive and selective detection of ppb-level H_2S, *J. Colloid Interface Sci.*, 2022, **627**, 332–342.

20 S. H. Shah, A. Azam and M. A. Rafiq, Atomistic simulations of CdS morphologies, *Cryst. Growth Des.*, 2015, **15**, 1792–1800.

21 X. Kong, F. Yu, H. Zhang, F. Lv, Y. Wang, L. Yin, J. Huang and Q. Feng, Synthesis and study of morphology regulation, formation mechanism and photocatalytic performance of CdS, *Appl. Surf. Sci.*, 2022, **576**, 151817.

22 C. Hsin, J. Liu and J. H. Wang, Spray-pyrolyzed thin film CdSe photoelectrochemical cells, *J. Electrochem. Soc.*, 1982, **129**, 719–722.

23 C. M. Shen, X. G. Zhang and H. L. Li, Influence of different deposition potentials on morphology and structure of CdSe films, *Appl. Surf. Sci.*, 2005, **240**, 34–41.

24 K. N. Shreekanthan, B. V. Rajendra, V. B. Kasturi and G. K. Shivakumar, Growth and characterization of semiconducting cadmium selenide thin films, *Cryst. Res. Technol.*, 2003, **38**, 30–33.

25 Y. Choi, M. Seol, W. Kim and K. Yong, Chemical bath deposition of stoichiometric CdSe quantum dots for efficient quantum-dot-sensitized solar cell application, *J. Phys. Chem. C*, 2014, **118**, 5664–5670.

26 F. Bai, K. Bian, X. Huang, Z. Wang and H. Fan, Pressure-induced nanoparticle phase behavior, property, and applications, *Chem. Rev.*, 2018, **119**, 7673–7717.

27 Z. Su, W. L. Shaw, Y. R. Miao, S. You, D. D. Dlott and K. S. Suslick, Shock wave chemistry in a metal–organic framework, *J. Am. Chem. Soc.*, 2017, **139**, 4619–4622.

28 Z. Dehghani, S. Nezamdoost, A. V. Noghreiyan and M. Nadafan, Influence of γ-irradiation on molecular structure and mass attenuation coefficients of γ-Al$_2$O$_3$ nanoparticles, *AIP Adv.*, 2023, **13**, 035120.

29 A. Sivakumar, L. Dai, S. Sahaya Jude Dhas, S. A. Martin Britto Dhas, V. Muthuvel, R. S. Kumar and A. I. Almansour, Acoustic shock wave recovery experiments on cubic zinc sulfide nanoparticles for electrical and magnetic switches applications, *Ceram. Int.*, 2024, **50**, 7418–7430.

30 A. Sivakumar, L. Dai, S. Sahaya Jude Dhas, S. A. Martin Britto Dhas, K. Kamala Bharathi, R. S. Kumar and A. I. Almansoure, Acoustic shockwave-induced solid-state morphological transformation of L-tyrosine, *CrystEngComm*, 2024, **26**, 1199–1205.

31 B. John and S. Varadharajaperumal, Comprehensive review on CdTe crystals: Growth, properties, and photovoltaic application, *Phys. Met. Metallogr.*, 2022, **2**, 180–196.

32 G. V. J. Dantas, N. P. de Moraes, R. Bacani and L. A. Rodrigues, Facile synthesis of cadmium sulfide and thermal annealing in N$_2$-rich atmosphere on Its Structural, Morphological, Chemical, and Optical Properties, *Mater. Chem. Phys.*, 2022, **277**, 125492.

33 N. B. Owen, P. L. Smith, J. E. Martin and A. J. Wright, X-ray diffraction at ultra-high pressures, *J. Phys. Chem. Solids*, 1963, **24**, 519–524.

34 B. Li, J. Xu, W. Chen, D. Fan, Y. Kuang, Z. Ye, W. Zhou and H. Xie, Phase transition and thermoelastic behavior of cadmium sulfide at high pressure and temperature, *J. Alloys Compd.*, 2018, **30**, 419–427.

35 A. Sivakumar, L. Dai, S. S. J. Dhas, S. A. Martin Britto Dhas, M. Vijayan, I. Kim, R. S. Kumar and A. I. Almansour, Acoustic shock wave-induced graphitic domains in amorphous carbon nanoparticles and Correlation Between Magnetic Response and Local Atomic Structures, *Diamond Relat. Mater.*, 2024, **141**, 110587.

36 S. Iqbal, N. A. Shaid, M. M. Sajid, Y. Javed, M. Fakhar-e-Alam, A. Mahmood, G. Ahmad, A. M. Afzal, S. Z. Hussain, F. Ali and M. Sarwar, Evaluation of structural and thermal properties of copper sulfide nanoparticles at different calcination temperatures, *J. Cryst. Growth*, 2020, **547**, 125823.

37 A. Sivakumar, L. Dai, S. S. J. Dhas, S. A. Martin Britto Dhas, R. S. Kumar and A. A. N. Raj, Acoustic shock wave induced chemical reactions in NaCl single crystal, *J. Mol. Struct.*, 2024, **1312**, 138490.

38 A. Sivakumar, L. Dai, S. A. Martin Britto Dhas, R. S. Kumar, V. Thangavel and V. N. Vijayakumar, Resistance of SiO$_2$ (α-cristobalite) to acoustic shock waves: Aerospace applications, *Ceram. Int.*, 2024, **50**, 17011–17019.

39 F. I. M. Bincy, S. Oviya, R. S. Kumar, P. Kanappan, I. Kim and S. A. Martin Britto Dhas, Acoustic shock wave-induced reversible phase transition in bismuth telluride, *J. Mater. Sci.*, 2024, **59**, 7044–7059.

40 S. Oviya, F. I. M. Bincy, R. S. Kumar, P. Kannappan, I. Kim and S. A. Martin Britto Dhas, Reversible phase transition and tunable band gap in zinc telluride via acoustic shock, *Dalton Trans.*, 2025, **54**, 3188–3206.

41 A. Sivakumar, L. Dai, S. S. J. Dhas, S. C. Lims and R. S. Kumar, Acoustic shock wave-induced B1 to B2 phase transition of CdO nanoparticles: Structure-property relationship and its mechanism in thermodynamic aspects, *Acta Mater.*, 2025, **286**, 120742.

42 S. Oviya, F. I. M. Bincy, S. Arumugam, K. K. Bharathi, R. S. Kumar, P. Kannappan, I. Kim and S. A. Martin Britto Dhas, Phase transition in indium selenide under acoustic shock for solar cell applications, *CrystEngComm*, 2024, **26**, 2498–2509.

43 F. I. M. Bincy, S. Oviya, R. S. Kumar, P. Kannappan, S. Arumugam, I. Kim and S. A. Martin Britto Dhas, Investigation of bismuth selenide's structural stability and tunable bandgap under exposure to acoustic shock waves for solar cell and aerospace applications, *Mech. Adv. Mater. Struct.*, 2024, 1–15.

44 S. Oviya, F. I. M. Bincy, R. S. Kumar, P. Kannappan, I. Kim and S. A. Martin Britto Dhas, Tuning the Band Gap of Bismuth Sulfide via Acoustic Shock Waves to Harness the Full Visible Spectrum for Enhanced Solar Cell Applications, *Mater. Chem. Phys.*, 2024, **333**, 130287.

45 K. P. J. Reddy and N. Sharath, Manually operated piston-driven shock tube, International Symposium on Shock Waves, *Curr. Sci.*, 2013, **104**, 172–175.

46 "WiSTL Wisconsin Shock Tube Laboratory, Gas Dynamics Calculator". Retrieved 6th June 2025, from **https://silver.neep.wisc.edu/~shock/tools/gdcalc.html**.

47 Y. Gao, D. Kong, J. Han, W. Zhou, Y. Gao, T. Wang and G. Lu, Cadmium sulfide *in situ* derived heterostructure hybrids with tunable component ratio for highly sensitive and selective detection of ppb-level H$_2$S, *J. Colloid Interface Sci.*, 2022, **627**, 332–342.

48 G. Anirudha, P. Sanhita and R. Satyabrata, Structural phase transformation from wurtzite to zinc-blende in uncapped CdS nanoparticles, *Solid State Commun.*, 2013, **154**, 25–29.

49 A. Sivakumar, L. Dai, S. S. J. Dhas, R. S. Kumar, A. I. Almansour and S. A. Martin Britto Dhas, Tuning of lower to higher crystalline nature of b-L-Glutamic acid by shock waves, *J. Mol. Struct.*, 2023, **1288**, 135788.

50 K. Ichiyanagi and K. G. Nakamura, Structural dynamics of materials under shock compression investigated with synchrotron radiation, *Metals*, 2016, **6**, 17.

51 B. Nasiri-Tabrizi, Thermal treatment effect on structural features of mechano-synthesized fluorapatite–titania nanocomposite: a comparative study, *J. Adv. Ceram.*, 2014, **3**, 31–42.

52 Z. Y. Liu, J. Li, J. F. Zhang, J. Li, P. T. Yang, S. Zhang, G. F. Chen, Y. Uwatoko, H. X. Yang, Y. Sui, K. Liu and J. G. Cheng, Quasi-one-dimensional superconductivity in the pressurized charge-density-wave conductor HfTe$_3$, *npj Quantum Mater.*, 2021, **6**, 90.

53 D. F. Zhi, B. Wen, Y. Sun, H. Xiang and Y. Zhou, Theoretical prediction on thermal and mechanical properties of high entropy $(Zr_{0.2}Hf_{0.2}Ti_{0.2}Nb_{0.2}Ta_{0.2})$ C by deep learning potential, *J. Mater. Sci. Technol.*, 2020, **43**, 168–174.

54 S. Ravi, D. P. Bisen, S. U. Shukla and B. G. Sharma, X-ray diffraction: a powerful method of characterizing nanomaterials, *Recent Res. Sci. Technol.*, 2012, **4**, 77–79.

55 S. Mnasri, S. A. B. Nasrallah, N. S. Fina, N. Bouarissa and M. Said, Electronic, lattice vibration and mechanical properties of CdTe, ZnTe, MnTe, MgTe, HgTe, and their ternary alloys, *Semicond. Sci. Technol.*, 2009, **24**, 095008.

56 T. Vijaya Kumar and K. V. Ramana, An effect of ball milling on microstructural parameters of nanostructured MoO_3-CuO-V_2O_5 composite nanopowders, *Int. J. Mech. Prod. Eng. Res. Dev.*, 2019, **9**, 131–142.

57 M. Basak, M. L. Rahman, M. F. Ahmed, B. Biswas and N. Sharmin, The use of X-ray diffraction peak profile analysis to determine the structural parameters of cobalt ferrite nanoparticles using Debye-Scherrer, Williamson-Hall, Halder-Wagner and Size-strain plot: Different precipitating agent approach, *J. Alloys Compd.*, 2022, **895**, 162694.

58 S. Ashok Kumar, S. S. R. Inbanathan, R. B. Vignesh, D. R. Rosaline, B. R. Kamalam, A. Uma, A. A. Ibrahim, S. Akbar, S. A. Martin Britto Dhas and S. Baskoutas, Shock wave pulsed strategy on green synthesized nickel oxide nanoparticles: Structural, morphological, and electrochemical performance, *Ceram. Int.*, 2024, **51**, 4509–4520.

59 C. O. Ehi-Eromosele, B. I. Ita and E. E. J. Iweala, Low-temperature combustion synthesis of cobalt magnesium ferrite magnetic nanoparticles effects of fuel-to-oxidizer ratio and sintering temperature, *J. Sol-Gel Sci. Technol.*, 2025, **76**, 298–308.

60 I. Fedorov, D. Korabelnikov, C. Nguyen and A. Prosekov, Physicochemical properties of L- and DL-valine: First-principles calculations, *Amino Acids*, 2020, **52**, 425–433.

61 A. Sivakumar, S. S. J. Dhas, L. Dai, V. Mowlika, P. Sivaprakash, R. S. Kumar, A. I. Almansour, S. Arumugam, I. Kim and S. A. Martin Britto Dhas, X-ray diffraction, and optical spectroscopic analysis on the crystallographic phase stability of shock wave loaded L-Valine, *J. Mater. Sci.*, 2023, **58**, 9210–9220.

62 J. Zhao, H. Liu, L. Ehm, D. Dong, Z. Chen and G. Gu, High-pressure phase transitions and amorphization in Bi_2Se_3, *J. Phys.: Condens. Matter*, 2013, **25**, 125602.

63 B. Azhdar, Influence of fuel-to-oxidizer ratio, potential of hydrogen and annealing temperature on the structural and optical properties of nanocrystalline MgO powders synthesized by the hydrothermal method, *J. Exp. Nanosci.*, 2023, **18**, 2276278–2276299.

64 P. Kumar, N. Saxena, R. Chandra, V. Gupta, A. Agarwal and D. Kanjilal, Nanotwinning and structural phase transition in CdS quantum dots, *Nanoscale Res. Lett.*, 2012, **7**, 584.

65 X. Zheng, Y. Song, J. Zhao, D. Tan, Y. Yang and C. Liu, Nanosecond time-resolved Raman spectroscopy of molecular solids under laser-driven shock compression, *Chem. Phys. Lett.*, 2010, **499**, 231–235.

66 K. Wakabayashi, T. Matsumura, Y. Nakayama, E. Yamada and M. Koshi, Temporal Change Of Raman Spectra Of Carbon Tetrachloride Under Laser-Driven Shock Compression, *AIP Conf. Proc.*, 2007, **955**, 1267–1272.

67 M. X. Gu, L. K. Pan, B. K. Tay and C. Q. Sun, Atomistic origin and temperature dependence of Raman optical red-shift in nanostructures: a broken bond rule, *J. Raman Spectrosc.*, 2007, **38**, 780–788.

68 J. Franken, S. A. Hambir, D. E. Hare and D. D. Dlott, Shock waves in molecular solids: ultrafast vibrational spectroscopy of the first nanosecond, *Shock Waves*, 1997, **7**, 135–145.

69 M. Pal, N. R. Mathews, P. Santiago and X. Mathew, A facile one-pot synthesis of highly luminescent CdS nanoparticles using thioglycerol as capping agent, *J. Nanopart. Res.*, 2012, **14**, 916.

70 J. Khatter and R. P. Chauhan, Gamma-ray induced modifications on CdS nanorod mesh: Structural, optical, and electrical properties, *Radiat. Phys. Chem.*, 2021, **182**, 109353.

71 X. Kong, F. Yu, H. Zhang, F. Lv, Y. Wang, L. Yin, J. Huang and Q. Feng, Synthesis and study of morphology regulation, formation mechanism and photocatalytic performance of CdS, *Appl. Surf. Sci.*, 2022, **576**, 151817.

72 Y. Kanemitsu, Y. Ishida, I. Nakada and H. Kuroda, Anomalous surface transformations in crystalline silicon induced by subpicosecond laser pulses, *Appl. Phys. Lett.*, 1986, **48**, 209–211.

73 M. Riaz, B. Ali, S. Mansoor Ali, M. I. Khan, M. Sana Ullah Sahar, M. Shahid and M. Alam, Stress-induced transformation on the cubic perovskite $RbTaO_3$ for high-temperature applications: a DFT approach, *J. Comput. Electron.*, 2024, **23**, 483–497.

74 M. Sharma, S. Murugavel, D. Kumar Shukla and F. M. F. de Groot, Reversal in lattice contraction of α-Fe_2O_3 nanoparticles, *J. Phys. Chem. C*, 2018, **122**, 9292–9301.

75 M. Sakar, R. M. Prakash and T. O. Do, Insights into the TiO_2-Based Photocatalytic Systems and Their Mechanisms, *Catalysts*, 2019, **9**, 680.

76 N. Khatun, E. G. Rini, P. Shirage, P. Rajput, S. N. Jha and S. Sen, Effect of lattice distortion on bandgap decrement due to vanadium substitution in TiO_2 nanoparticles, *Mater. Sci. Semicond. Process.*, 2016, **50**, 7–13.

77 R. Sreekumar, R. Jayakrishnan, C. S. Kartha, K. P. Vijayakumar, S. A. Khan and D. K. Avasthi, Enhancement of band gap and photoconductivity in gamma indium selenide due to swift heavy ion irradiation, *J. Appl. Phys.*, 2008, **103**, 023709.

78 S. Mathew, S. A. Joseph and P. Radhakrishnan, Shifting of Fluorescence Peak in CdS Nanoparticles by Excitation Wavelength Change, *J. Fluoresc.*, 2011, **21**, 1479–1484.

79 J. Khatter and R. P. Chauhan, Effect of temperature on properties of cadmium sulfide nanostructures synthesized by solvothermal method, *J. Mater. Sci.: Mater. Electron.*, 2020, **31**, 2676–2685.

80 E. Gharibshahi, Synthesis and Optical Properties of Cadmium Telluride (CdTe) Semiconductor Nanoparticles, *Solid State Commun.*, 2020, **320**, 114009.

81 C. Hu, X. Zeng, J. Cui, H. Chen and J. Lu, Size effects of Raman and photoluminescence spectra of CdS nanobelts, *J. Phys. Chem. C*, 2013, **117**, 20998–21005.

82 D. Han, G. Yue, K. Wang, J. Baugh and Y. Wu, Nanovoid-related large redshift of photoluminescence peak energy in hydrogenated amorphous silicon, *Appl. Phys. Lett.*, 2002, **80**, 40–42.

83 S. P. Fu, Y. F. Chen and K. Tan, Recombination mechanism of photoluminescence in InN epilayers, *Solid State Commun.*, 2006, **137**, 203–207.

84 Z. Fang, H. He, L. Gan, J. Li and Z. Ye, Understanding the Role of Lithium Doping in Reducing Nonradiative Loss in Lead Halide Perovskites, *Adv. Sci.*, 2018, **5**, 1800736.

85 K. D. Jons, R. Hafenbrak, R. Singh, F. Ding, J. D. Plumhof, A. Rastelli, O. G. Schmidt, G. Bester and P. Michler, Dependence of the redshifted and blue-shifted photoluminescence spectra of single InxGa1- xAs/GaAs quantum dots on the applied uniaxial stress, *Phys. Rev. Lett.*, 2011, **107**, 217402.

86 J. A. Suchikova, V. V. Kidalov and G. A. Sukach, Blue shift of photoluminescence spectrum of porous InP, *ECS Trans.*, 2010, **25**, 59–64.

87 V. P. N. Nampoori, C. P. G. Vallabhan, O. Vigil, I. Riech, M. Garcia-Rocha and O. Zelaya-Angel, Characterization of defect levels in chemically deposited CdS films in the cubic-to-hexagonal phase transition, *J. Vac. Sci. Technol., A*, 1997, **15**, 2282–2286.

88 S. Khajuria, S. Sanotra, J. Ladol and H. N. Sheikh, Synthesis, characterization and optical properties of cobalt and lanthanide doped CdS nanoparticles, *J. Mater. Sci.: Mater. Electron.*, 2015, **26**, 7073–7080.

89 H. Zeng, G. Duan, Y. Li, S. Yang, X. Xu and W. Cai, Blue luminescence of ZnO nanoparticles based on non-equilibrium processes defect origins and emission controls, *Adv. Funct. Mater.*, 2010, **20**, 561–572.

90 Y. C. Liang and T. W. Lung, Growth of Hydrothermally Derived CdS Based Nanostructures with Various Crystal Features and Photoactivated Properties, *Nanoscale Res. Lett.*, 2016, **11**, 264.

91 Y. I. Meshcheryakov, A. K. Divakov, S. A. Atroshenko and N. S. Naumova, Effect of velocity nonuniformity on the dynamic recrystallization of metals in shock waves, *Tech. Phys. Lett.*, 2010, **36**, 1125–1128.

92 Y. Su, D. Ao, H. Liu and Y. Wang, Effect of velocity nonuniformity on the dynamic recrystallization of metals in shock waves, *J. Mater. Chem. A*, 2017, **5**, 8680–8689.

93 A. Sivakumar, L. Dai, S. Sahaya Jude Dhas, S. A. Martin Britto Dhas, P. Eniya, R. S. Kumar and A. I. Almansour, Experimental Evidence of Acoustic Shock Wave-Induced Dynamic Recrystallization: A Case Study on Ammonium Sulfate, *Cryst. Growth Des.*, 2024, **24**, 491–498.

94 A. Sivakumar, L. Dai, S. Sahaya Jude Dhas, S. A. Martin Britto Dhas, S. Laha, R. S. Kumar and A. I. Almansour, Acoustic Shock Wave-Induced Solid-State Fusion of Nanoparticles: A Case Study of the Conversion of One-Dimensional Rod Shape into three-Dimensional Honeycomb Nanostructures of CdO for High-Performance Energy Storage Materials, *Inorg. Chem.*, 2024, **63**, 576–592.

95 S. Rajkumar, R. G. Devaraj, P. Abhishek, R. S. Sinha, S. E. Muthu, A. Barrathi and S. Arumugam, Enhancing photocatalytic dye degradation efficiency through the utilization of shock wave effects on neodymium oxide (Nd_2O_3), *J. Mol. Struct.*, 2024, **1318**, 139215.